Scripta Materialia 194 (2021) 113698

Contents lists available at ScienceDirect

Scripta Materialia

journal homepage: www.elsevier.com/locate/scriptamat

On the non-classical crystallographic slip in $Ti_{n+1}AlC_n$ MAX phases

Zhiqiang Zhan[a], Miladin Radovic[a,*], Ankit Srivastava[a,*]

[a] Department of Materials Science and Engineering, Texas A&M University, College Station, TX, USA

ARTICLE INFO

Article history:
Received 22 September 2020
Revised 20 December 2020
Accepted 23 December 2020
Available online 4 January 2021

Keywords:
Compression test
Plastic deformation
Slip
Layered structures
MAX phase

ABSTRACT

In this work, we investigate the effect of atomic stacking on non-classical (non-Schmid) crystallographic slip in a class of atomically layered ternary carbides referred to as MAX phases with general formula $M_{n+1}AX_n$, where the value of n represents the stacking sequence. To this end, we have carried out compression tests on single crystal micropillars of Ti_3AlC_2 with a range of crystallographic orientations and compared the results with that of Ti_2AlC. Our results show that similar to Ti_2AlC, Ti_3AlC_2 also exhibits non-classical crystallographic slip, wherein the crystallographic slip depends on both the resolved shear stress and the stress normal to the slip plane. However, for crystallographic slip, the intrinsic critical resolved shear stress in Ti_3AlC_2 is greater than Ti_2AlC, while the frictional resistance in Ti_3AlC_2 is smaller than Ti_2AlC. The implications of these findings on the macroscopic response of polycrystalline aggregates of these two MAX phases is also discussed.

MAX phases are a family of ternary carbides and nitrides with general formula $M_{n+1}AX_n$, where n ranges from 1-3, M is an early transitional metal, A is mostly an element from groups 13-16, and X is carbon or nitrogen [1,2]. MAX phases have hexagonal crystal structure (space group P63/mmc), where M elements are close packed, the X atoms fill in the octahedral sites to form M_6X- octahedra in the $M_{n+1}X_n$ layers that are interleaved with A layers [1]. Different values of n in the formula represents the stacking sequence of MAX phases; for example, when n = 1, one $M_{n+1}X_n$ layer (or two M layers) separate the A layers and so on. Due to the unique layered crystal structure and a combination of atomic bonds within it, MAX phases are endowed with useful properties such as good thermal stability, high specific stiffness, good machinability, thermal and electrical conductivity, thermal shock resistance and damage tolerance, while some are also oxidation resistance [1,3].

Until recently our understanding of the mechanical behavior of MAX phases was solely based on the mechanical testing of their polycrystalline aggregates. Numerous studies on polycrystalline MAX phases showed that unlike their counterpart binary carbides (MX), MAX phases, even at room temperature, behave in pseudo-ductile manner due to crystallographic slip on basal slip systems [4–8] and kinking [6–13]. The studies on polycrystalline MAX phases have also highlighted the strong influence of the microstructural features such as grain morphology and size [11,12,14]. In particular, it has been shown that textured polycrystalline MAX phases at room temperature can exhibit very ductile response under compression with strain to failure exceeding 10% [8]. Thus, it is important to understand the single-crystal level mechanical response of MAX phases. Recent, micropillar compression experiments have enabled us to study crystallographic slip on the single crystal level, which is challenging to deconvolute from mechanical testing of polycrystalline aggregates due to simultaneous activation of multiple mechanisms as well as the strong effect of the microstructural parameters on stress distribution in polycrystals [11,12,14–17].

Early micropillar compression tests on Ti_2InC [15], Ti_4AlN_3 [15] and Ti_3SiC_2 [16] MAX phases have shown that depending on the crystallographic orientation the material either undergoes basal slip or cleavage, wherein the onset of yielding due to basal slip was found to be extremely orientation dependent. More recently, Zhan et al. [17] carried out extensive micropillar compression tests of Ti_2AlC MAX phase and showed that unlike in the case of most materials that obey a classical Schmid law, the critical resolved shear stress (τ_{CRSS}) for the onset of basal slip in Ti_2AlC is highly orientation dependent. This non-classical orientation dependence of τ_{CRSS} in Zhan et al. [17] was attributed to the strong effect of the presence of stress normal to the basal plane (σ_{norm}) on the onset of basal slip. The dependence of τ_{CRSS} on σ_{norm} was shown to follow, $\tau_{CRSS} = k\sigma_{norm} + \tau_0$, with the value of k characterizing the frictional resistance for basal slip and τ_0 being the intrinsic critical resolved shear stress for basal slip.

The recent observation of non-classical crystallographic slip in Ti_2AlC MAX phase raises a fundamental question: How does the

* Corresponding authors.
E-mail addresses: mradovic@tamu.edu (M. Radovic), ankit.sri@tamu.edu (A. Srivastava).

https://doi.org/10.1016/j.scriptamat.2020.113698
1359-6462/

atomic stacking affect the non-classical crystallographic slip in MAX phases? To answer this question, herein, we analyzed the effect of the atomic stacking of MAX phases on crystallographic slip by carrying out a series of micropillar compression tests of Ti_3AlC_2 MAX phase and comparing them to those reported for Ti_2AlC [17]. The major difference between these two MAX phases lies in their atomic stacking: in Ti_2AlC one layer of Ti_6C octahedra are separated by a single atomic Al layer, while in Ti_3AlC_2 two layers of Ti_6C octahedra are separated by a single atomic Al layer. These aluminum-based MAX phases are some of the most promising structural materials for high temperature applications due to their high oxidation resistance provided by self-forming Al_2O_3 layer [18–20]. Our results show that Ti_3AlC_2 also exhibits non-classical crystallographic slip as Ti_2AlC, however, with higher intrinsic critical resolved shear stress and smaller frictional resistance when compared to Ti_2AlC. So that even for the same set of crystallographic orientations, a Ti_3AlC_2 crystal is not always plastically harder or softer than the corresponding Ti_2AlC crystal.

In this work, fully dense polycrystalline Ti_3AlC_2 sample was sintered by pulsed electric current sintering following a procedure described in detail in ref. [21]. Ti_3AlC_2 bulk sample was then annealed in a tube furnace at 1300 °C for 48 h to obtain large grains. Subsequently, the sample was ground and polished up to 0.1 μm diamond suspension and fine polished with 0.025 μm colloidal silica. The polished specimen surface was characterized by Electron Backscattered Diffraction (EBSD) with a spatial resolution of $\approx$ 1.5 μm (FERA-3, Tescan) to determine crystallographic orientation of the grains in selected areas. Next, micropillars were milled from large individual grains of known crystallographic orientations using 30 keV Ga source Focused Ion Beam (Lyra-3, Tescan). The final micropillars had top diameter of $\approx$ 10 μm and height of $\approx$ 20 μm with average vertical taper $<$ 5°. Micropillar compression test in air and at room temperature were then carried out using a nanoindenter (Hysitron TI 950) equipped with a 20 μm diameter diamond flat punch. The compression tests were carried out in force-controlled mode with 0.3 mN/s loading rate. The micropillar dimensions and the loading conditions are same as in ref. [17]. The load – displacement data obtained from the nanoindenter were converted to engineering stress – strain curves, where the engineering stress was calculated by normalizing the load with average micropillar diameters taken at the top and the mid-section. The deformed structures of the micropillars were also characterized by Scanning Electron Microscopy (SEM) in Secondary Electron (SE) mode (FERA-3, Tescan).

Several micropillars were milled from large grains of Ti_3AlC_2 specimen. The locations of different micropillars are marked on the EBSD maps and the associated color-coded stereographic triangle in Figs. 1(a) and (b), respectively, and a selected but typical as-milled micropillar is shown in Fig. 1(c). The crystallographic orientation in terms of Euler angles $(\varphi_1, \phi, \varphi_2)$ of all micropillars are given in Table 1. In MAX phases only two independent basal slip systems, $\{0001\}\langle 11\bar{2}0\rangle$, are operative and accordingly the maximum Schmid factor, $\mu^{\alpha}_{max} = \max(|\mu^{\alpha}|)$, (where μ^{α} is the Schmid factor for α^{th} basal slip system) for all micropillars are estimated as in ref. [17] and are given in Table 1. The maximum Schmid factor for basal slip system for all the micropillars considered in this work vary in the range 0.24 to 0.50.

The engineering compressive stress-strain curves for selected micropillars are shown in Fig. 2(a). The numbers marked on the figure are consistent with the micropillar numbers in Fig. 1 and Table 1. Some of the micropillars such as micropillars 2, 6 and 7 were deformed to a compressive strain more than 2.5% and post-deformation SEM image of these micropillars are shown in Figs. 2(c)-(e). The post-deformation SEM images of the micropillars confirm that the micropillars of Ti_3AlC_2 under compression deform by crystallographic slip on multiple parallel slip planes. The

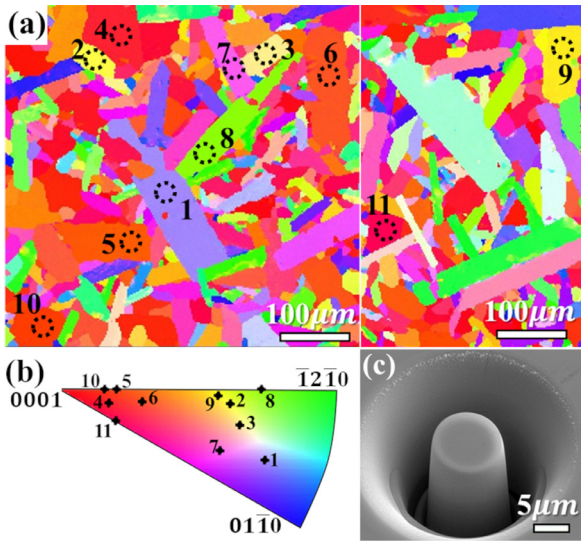

Fig. 1. (a) EBSD inverse pole figure (IPF) maps showing the microstructure of Ti_3AlC_2 MAX phase wherein the dotted circles mark the location of micropillars that were milled from these grains. (b) The associated color-coded stereographic triangle wherein the crystallographic orientation of the grains from which the micropillars were milled are marked. (c) A selected but typical SE-SEM image of an as-milled micropillar.

Table 1
Euler angles $(\varphi_1, \phi, \varphi_2)$ and maximum Schmid factor for $\{0001\}\langle 11\bar{2}0\rangle$ slip system for all the micropillars.

Micropillars	Max. Schmid Factor	Euler Angles		
		φ_1	ϕ	φ_2
1	0.34	119.0°	66.7°	19.6°
2	0.49	157.0°	129.0°	6.2°
3	0.46	37.0°	55.6°	11.1°
4	0.28	96.5°	162.0°	42.7°
5	0.32	176.5°	159.8°	1.3°
6	0.38	96.2°	25.2°	51.4°
7	0.45	116.3°	51.7°	21.9°
8	0.42	48.7°	118.7°	0.8°
9	0.50	86.0°	134.3°	3.3°
10	0.24	51.8°	165.6°	58.6°
11	0.27	83.7°	160.8°	30.0°

compressive deformation of other micropillars such as micropillars 4, 5 and 9 were interrupted within 2.5% strain. The compressive stress-strain response of all tested micropillars have three characteristic stages. Initially, the stress-strain response of the micropillars is linear and with continued deformation the stress-strain response deviates from the linearity which marks the onset of yielding, Fig. 2(b). Post-yielding, the stress-strain response shows brief period of hardening that eventually saturates with continued deformation. The onset of yielding i.e. yield stress (σ_0) from the stress-strain response of micropillars is identified as the 0.015% offset of the average slope of the initial linear portion as shown in Fig. 2(b). For micropillar 4, $\sigma_0 \approx 177$ MPa while for micropillar 9, $\sigma_0 \approx 56$ MPa. These lead to a critical resolved shear stress, $\tau_{CRSS} = \sigma_0 \times \mu^{\alpha}_{max}$, value of $\approx$ 49.7 MPa for micropillar 4 and $\approx$ 27.9 MPa for micropillar 9. Thus, the value of τ_{CRSS} for Ti_3AlC_2 is different for different crystallographic orientations, which confirms that similar to Ti_2AlC [17], the crystallographic slip in Ti_3AlC_2 does not follow the classical Schmid's law. Note that the classical Schmid's law states that the value of τ_{CRSS} is a material property and is not dependent upon the crystallographic orientation.

Next, we compare the stress-strain response of micropillars of Ti_3AlC_2 and Ti_2AlC MAX phases with similar crystallographic orientations. The stress-strain response of two pairs of micropillars

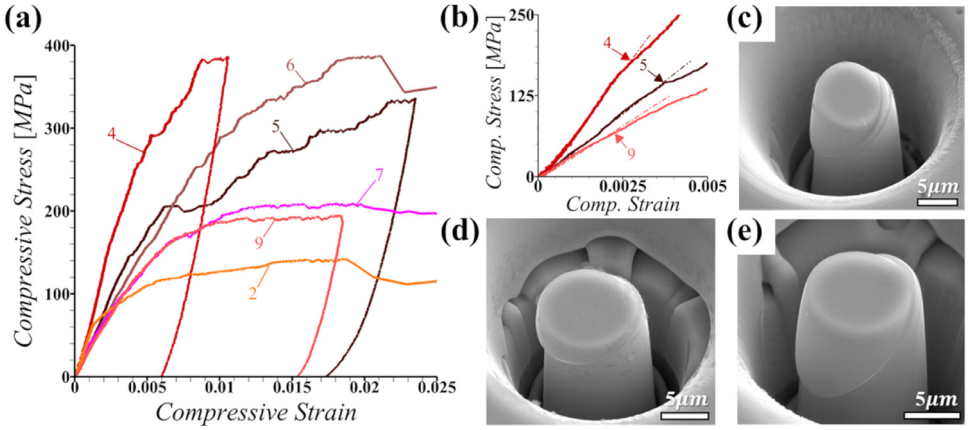

Fig. 2. (a) The engineering compressive stress-strain curves for selected micropillars. The crystallographic orientation of the numbered micropillars are given in Table 1. (b) Early stage of engineering compressive stress-strain curves showing the onset of yielding in the stress-strain response of three micropillars. The dash-dot lines in (b) mark the initial linear portion of the stress-strain curves. SE-SEM images of the deformed micropillars milled from (c) grain number 2, (d) grain number 6 and (e) grain number 7.

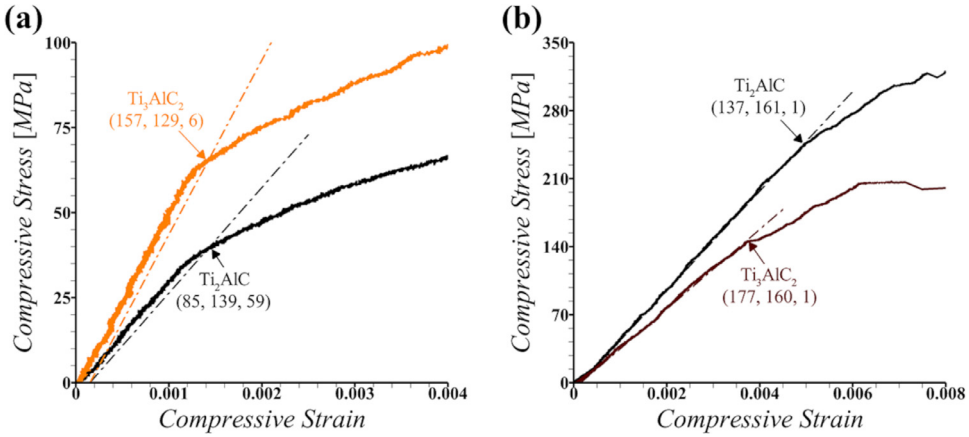

Fig. 3. A comparison of the engineering compressive stress-strain response of Ti_3AlC_2 and Ti_2AlC micropillars with maximum Schmid factor for basal slip systems (a) ≈ 0.5 and (b) ≈ 0.32. The crystallographic orientation in terms of Euler angles (in degrees) of each micropillar is also given in the figure. The stress-strain response of Ti_2AlC micropillars are reproduced from the work of Zhan et al. [17].

of Ti_3AlC_2 and Ti_2AlC with crystallographic orientations that result in roughly the same maximum Schmid factors for basal slip are compared in Fig. 3. In Fig. 3(a), the maximum Schmid factor is ≈ 0.49 for the Ti_3AlC_2 micropillar (micropillar 2) while it is ≈ 0.5 for the Ti_2AlC micropillar (micropillar Y1 in ref. [17]). From the stress-strain curve in Fig. 3(a), the yield stress is ≈ 65.7 MPa for the Ti_3AlC_2 micropillar which is higher than the yield stress of ≈ 39 MPa for the Ti_2AlC micropillar. Similarly, in Fig 3(b), the maximum Schmid factor is ≈ 0.32 for the Ti_3AlC_2 micropillar (micropillar 5) while it is ≈ 0.31 for the Ti_2AlC micropillar (micropillar O1 in ref. [17]). However, unlike the high Schmid factor case, for this relatively lower Schmid factor case, yield stress for the Ti_3AlC_2 micropillar is ≈ 145.5 MPa which is lower than the yield stress of ≈ 245.6 MPa for the Ti_2AlC micropillar.

From the micropillar compression tests of Ti_2AlC MAX phase in Zhan et al. [17] it was shown that Ti_2AlC follows non-classical crystallographic slip wherein the basal slip is not only dependent upon the resolved shear stress, τ_{RSS}, but also on the stress acting normal to the basal plane, σ_{norm}, Fig. 4(a). This in turn leads to the critical resolved shear stress, τ_{CRSS}, required to initiate basal slip being dependent upon σ_{norm} such that $\tau_{CRSS} = k\sigma_{norm} + \tau_0$, where k is the frictional coefficient for the basal slip and τ_0 is the intrinsic critical resolved shear stress for basal slip. Following this model, we plot in Fig. 4(b) the variation of τ_{CRSS} with σ_{norm} for all the Ti_3AlC_2 micropillars considered in this work together with the results for the Ti_2AlC micropillars from ref. [17]. In Fig. 4(b), $\tau_{CRSS} = \sigma_0 \cos\phi \cos\lambda$ and $\sigma_{norm} = \sigma_0 \cos^2\phi$, where ϕ is the angle between the basal plane normal and the loading direction, λ is the angle between the active slip direction and the loading direction, and σ_0 is the 0.015% offset yield strength for the micropillars of both Ti_3AlC_2 and Ti_2AlC. As shown in Fig. 4(b), similar to Ti_2AlC, the variation of τ_{CRSS} with σ_{norm} for Ti_3AlC_2 can also be represented as $\tau_{CRSS} = k\sigma_{norm} + \tau_0$, with frictional coefficient for the basal slip, $k = 0.20$, and the intrinsic critical resolved shear stress, $\tau_0 = 19.6$ MPa. This shows that both Ti_3AlC_2 and Ti_2AlC qualitatively follow a non-classical mechanism of crystallographic slip. However, due to the difference in their atomic stacking, quantitatively, the frictional coefficient for the basal slip in Ti_3AlC_2 is roughly 28.6% smaller than that in Ti_2AlC while the intrinsic critical resolved shear stress for the basal slip in Ti_3AlC_2 is roughly 42% greater than that in Ti_2AlC.

Prior works on polycrystalline aggregates of MAX phases have also shown that their mechanical properties and hysteretic response under cyclic loading does significantly depend on the atomic stacking. For example, it has been shown that the Ti_3AlC_2 is stiffer than Ti_2AlC [22–24], and for comparable grain sizes Ti_3AlC_2 has slightly higher compressive strength than Ti_2AlC [11,21]. While energy dissipation under cyclic loading i.e. the size of the hysteretic loop is shown to be greater for Ti_2AlC compared to Ti_3AlC_2 [25]. The initial yield point of a polycrystalline aggregate is largely controlled by the onset of crystallographic slip in the grains that are oriented for easy slip. Thus, our finding that the intrinsic value

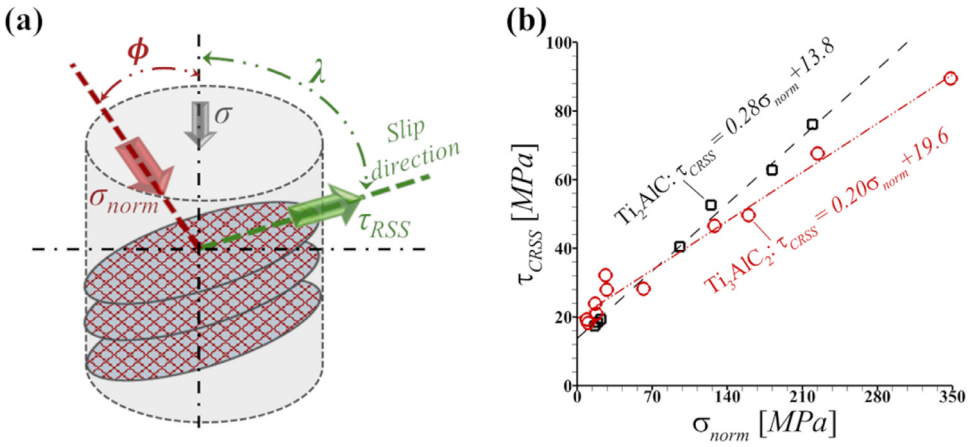

Fig. 4. (a) A schematic showing applied uniaxial compressive stress, σ, on a cylindrical specimen, resultant normal stress, σ_{norm}, acting on the slip plane with plane normal inclined at an angle ϕ to the compression axis and resolved shear stress, τ_{RSS}, acting on the same slip plane in the slip direction with angle of inclination λ with respect to the compression axis. (b) The variation of critical resolved shear stress, τ_{CRSS}, (i.e. the value of τ_{RSS} at the onset of yielding in the stress-strain response of micropillars), with σ_{norm} for both Ti_3AlC_2 and Ti_2AlC micropillars. The data for Ti_2AlC are reproduced from the work of Zhan et al. [17].

of τ_{CRSS} i.e. the value of τ_0 is greater for Ti_3AlC_2 compared to Ti_2AlC, to an extent, rationalizes the observed difference in the strength levels of these two MAX phases. On the other hand, the hysteretic response of MAX phases during loading-unloading cycles is associated with reversible plastic flow due to continual buildup and relaxation of large incompatibility stresses in the material [26,27]. In line with this micromechanism, our finding that the value of k which represents the frictional resistance for the basal slip is greater for Ti_2AlC compared to Ti_3AlC_2, to an extent, rationalizes the greater energy dissipation under cyclic loading for Ti_2AlC compared to Ti_3AlC_2.

In summary, we have shown that Ti_3AlC_2 also exhibits non-classical crystallographic slip as Ti_2AlC, however, with higher intrinsic critical resolved shear stress and smaller frictional resistance when compared to Ti_2AlC. Although, the primary difference between Ti_2AlC and Ti_3AlC_2 is the number of layers of Ti_6C octahedra that are separated by an atomic layer of Al, the difference in the number of Ti_6C octahedra layers also affects the Ti-Al bonds in $Ti_{n+1}AlC_n$ [28–30]. Thus, in MAX phases where the crystallographic slip is postulated to predominantly occur between the weakly bonded M-A layers [31], it is not surprising that the atomic stacking affects the crystallographic slip in these materials. Nevertheless, the effect of atomic stacking on the nature of the non-classical crystallographic slip in $Ti_{n+1}AlC_n$ MAX phases was not at all intuitive a priori. The effect of atomic stacking on the non-classical crystallographic slip presented here (to some extent) also rationalizes the observed differences in yielding under monotonic loading and hysteretic response under cyclic loading of polycrystalline aggregates of the two MAX phases. We note that the non-classical crystallographic slip (violation of Schmid's law) has been previously observed in bcc metals [32–36] due to non-planar spreading of screw dislocation core in the presence of stresses other than the resolved shear stress [35] as a possible atomic-scale mechanism. At present, however, the atomic-scale origin of non-classical crystallographic slip in MAX phases is not clear and we hope that our results will instigate future works in this direction.

Declaration of Competing Interest

The authors declare that they have no known competing financial interests or personal relationships that could have appeared to influence the work reported in this paper.

Acknowledgments

The financial support provided by the U.S. National Science Foundation grants CMMI – 1729350 and CMMI – 1944496 are gratefully acknowledged.

References

[1] M.W. Barsoum, M. Radovic, Annu. Rev. Mater. Res. 41 (1) (2011) 195–227.
[2] M. Sokol, V. Natu, S. Kota, M.W. Barsoum, Trends Chem. 1 (2) (2019) 210–223.
[3] M. Radovic, M.W. Barsoum, Am. Ceram. Soc. Bull. 92 (3) (2013) 20–27.
[4] L. Farber, M.W. Barsoum, A. Zavaliangos, T. El-Raghy, I. Levin, J. Am. Ceram. Soc. 81 (6) (1998) 1677–1681.
[5] M.W. Barsoum, L. Farber, I. Levin, A. Procopio, T. El-Raghy, A. Berner, J. Am. Ceram. Soc. 82 (9) (1999) 2545–2547.
[6] M.W. Barsoum, L. Farber, T. El-Raghy, Metall. Mater. Trans. A 30 (7) (1999) 1727–1738.
[7] L. Farber, I. Levin, M.W. Barsoum, Philos. Mag. Lett. 79 (4) (1999) 163–170.
[8] M.W. Barsoum, T. El-Raghy, Metall. Mater. Trans. A 30 (2) (1999) 363–369.
[9] J.M. Molina-Aldareguia, J. Emmerlich, J.-P. Palmquist, U. Jansson, L. Hultman, Scr. Mater. 49 (2) (2003) 155–160.
[10] B.J. Kooi, R.J. Poppen, N.J.M. Carvalho, J.T.M. De Hosson, M.W. Barsoum, Acta Mater. 51 (10) (2003) 2859–2872.
[11] R. Benitez, H. Gao, M. O'Neal, P. Lovelace, G. Proust, M. Radovic, Acta Mater. 143 (2018) 130–140.
[12] R. Benitez, W.H. Kan, H. Gao, M. O'Neal, G. Proust, A. Srivastava, M. Radovic, Acta Mater. 189 (2020) 154–165.
[13] M. Barsoum, T. Zhen, S. Kalidindi, M. Radovic, A. Murugaiah, Nat. Mater. 2 (2) (2003) 107–111.
[14] A. Guitton, S. Van Petegem, C. Tromas, A. Joulain, H. Van Swygenhoven, L. Thilly, Appl. Phys. Lett. 104 (24) (2014) 241910.
[15] C. Brüsewitz, I. Knorr, H. Hofsäss, M.W. Barsoum, C.A. Volkert, Scr. Mater. 69 (4) (2013) 303–306.
[16] M. Higashi, S. Momono, K. Kishida, N.L. Okamoto, H. Inui, Acta Mater. 161 (2018) 161–170.
[17] Z. Zhan, Y. Chen, M. Radovic, A. Srivastava, Mater. Res. Lett. 8 (7) (2020) 275–281.
[18] M.W. Barsoum, M. Ali, T. El-Raghy, Metall. Mater. Trans. A 31 (7) (2000) 1857–1865.
[19] X.H. Wang, Y.C. Zhou, J. Mater. Sci. Technol. 26 (5) (2010) 385–416.
[20] S. Basu, N. Obando, A. Gowdy, I. Karaman, M. Radovic, J. Electrochem. Soc. 159 (2) (2012) C90–C96.
[21] H. Gao, R. Benitez, W. Son, R. Arroyave, M. Radovic, Mater. Sci. Eng. 676 (2016) 197–208.
[22] J. Wang, Y. Zhou, Phys. Rev. B 69 (21) (2004).
[23] M. Radovic, M.W. Barsoum, A. Ganguly, T. Zhen, P. Finkel, S.R. Kalidindi, E. Lara-Curzio, Acta Mater. 54 (10) (2006) 2757–2767.
[24] P. Finkel, M.W. Barsoum, T. El-Raghy, J. Appl. Phys. 87 (4) (2000) 1701–1703.
[25] A.G. Zhou, M.W. Barsoum, J. Alloys Compd. 498 (1) (2010) 62–70.
[26] N.G. Jones, C. Humphrey, L.D. Connor, O. Wilhelmsson, L. Hultman, H.J. Stone, F. Giuliani, W.J. Clegg, Acta Mater. 69 (2014) 149–161.
[27] R. Benitez, W.H. Kan, H. Gao, M. O'Neal, G. Proust, M. Radovic, Acta Mater. 105 (2016) 294–305.
[28] N.J. Lane, S.C. Vogel, E.a.N. Caspi, M.W. Barsoum, J. Appl. Phys. 113 (18) (2013) 183519.

[29] J. Tan, H. Han, D. Wickramaratne, W. Liu, M. Zhao, P. Huai, J. Phys. D Appl. Phys. 47 (21) (2014) 215301.
[30] J. Xiao, T. Yang, C. Wang, J. Xue, Y. Wang, J. Am. Ceram. Soc. 98 (4) (2015) 1323–1331.
[31] K. Gouriet, P. Carrez, P. Cordier, A. Guitton, A. Joulain, L. Thilly, C. Tromas, Philos. Mag. 95 (23) (2015) 2539–2552.
[32] J. Christian, Metall. Trans. A 14 (7) (1983) 1237–1256.
[33] G. Taylor, Prog. Mater Sci. 36 (1992) 29–61.
[34] Q. Qin, J.L. Bassani, J. Mech. Phys. Solids 40 (4) (1992) 813–833.
[35] M.a.-S. Duesbery, V. Vitek, Acta Mater. 46 (5) (1998) 1481–1492.
[36] A. Srivastava, H. Ghassemi-Armaki, H. Sung, P. Chen, S. Kumar, A.F. Bower, J. Mech. Phys. Solids 78 (2015) 46–69.